Journal of Solid State Chemistry 184 (2011) 1176–1185

Contents lists available at ScienceDirect

Journal of Solid State Chemistry

journal homepage: www.elsevier.com/locate/jssc

Crystal structure, characterization and thermoelectric properties of the type-I clathrate $Ba_{8-y}Sr_yAl_{14}Si_{32}$ $(0.6 \leq y \leq 1.3)$ prepared by aluminum flux

John H. Roudebush [a], Eric S. Toberer [b], Håkon Hope [a], G. Jeffrey Snyder [b], Susan M. Kauzlarich [a,*]

[a] Department of Chemistry, University of California, Davis, One Shields Avenue, Davis, CA 95616, USA
[b] Materials Science, California Institute of Technology, 1200 East California Boulevard, Pasadena, CA 91125, USA

ARTICLE INFO

Article history:
Received 11 December 2010
Received in revised form
18 February 2011
Accepted 27 February 2011
Available online 8 March 2011

Keywords:
Thermoelectric properties
Zintl phase
Low temperature X-ray diffraction
12 K structure
Inorganic clathrate
$Ba_8Al_{16}Si_{30}$
Clathrate type-I

ABSTRACT

The title compound was prepared as single crystals using an aluminum flux technique. Single crystal and powder X-ray diffraction indicate that this composition crystallizes in the clathrate type-I structure, space group $Pm\bar{3}n$. Electron microprobe characterization indicates the composition to be $Ba_{8-y}Sr_yAl_{14.2(2)}Si_{31.8(2)}$ $(0.77 < y < 1.3)$. Single-crystal X-ray diffraction data (90 and 12 K) were refined with the Al content fixed at the microprobe value (12 K data: $R_1 = 0.0233$, $wR_2 = 0.0441$) on a crystal of compositions Ba. The Sr atom preferentially occupies the 2*a* position; mixed Al/Si occupancy was found on all framework sites. These refinements are consistent with a fully occupied framework and nearly fully occupied cation guest sites as found by microprobe analysis. Temperature dependent electrical resistivity and thermal conductivity have been measured from room temperature to 1200 K on a hot-pressed pellet. Electrical resistivity reveals metallic behavior. The negative Seebeck coefficient indicates transport processes dominated by electrons as carriers. Thermal conductivity is between 22 and 25 mW/cm K. The sample shows n-type conductivity with a maximum figure of merit, *zT* of 0.3 at 1200 K. A single parabolic band model predicts a five-fold increase in *zT* at 800 K if carrier concentration is lowered.

1. Introduction

The study of thermoelectric materials is a widely researched field because of the potential role these materials can play to increase the efficiency of the global energy infrastructure, primarily through the recovery of waste heat [1,2]. Although electric motors have begun to emerge in consumer automobiles, the internal combustion engine continues to be used and developed for most industrial transportation applications. Thermoelectric devices can be used to capture the waste heat from these engines and convert it into electricity, thereby increasing efficiency [1]. The ideal thermoelectric device for transportation applications has good heat conversion efficiency across the temperature range of the heat source, is easy and inexpensive to process, is lightweight and is formed from readily available materials. A thermoelectric material made primarily from period 3 elements such as aluminum and silicon has the potential to meet these requirements.

To achieve a good conversion of heat to electricity, a thermoelectric material must have a high Seebeck coefficient (S), high electrical conductivity (σ) and low thermal conductivity (κ). These properties combine to measure the dimensionless figure of merit of the material, *zT*, ($zT = S^2T\sigma/\kappa$). One avenue of current research has focused on increasing *zT* through the lowering of thermal conductivity, even beyond that of vitreous SiO_2, by accessing phonon scattering modes with the low frequency vibration of heavy atoms [1–6]. However, as the temperature increases, S becomes the dominant contribution in the *zT* equation. Since the Seebeck coefficient is squared in the *zT* equation ($zT = S^2\sigma T/\kappa$), thermoelectric materials with high melting points and sufficiently large band gaps will be able to take advantage of the exponential contribution of S to achieve high *zT* values without the addition of heavy elements.

Inorganic clathrate-structured materials are of interest to the thermoelectric community because of their high *zT* values, arising from good electronic mobility and low lattice thermal conductivity. Additionally, the complexity of their unit cells allows for the tuning of the bulk materials properties by doping elements and/or through subtle synthetic adjustments [7,8]. Compounds crystallizing in the clathrate structure types (referred to as type-I, -II, -III, and so on) have the general form of a covalently bonded framework of polyhedra in which an atom is encapsulated. The covalently bonded framework promotes high electron mobility, leading to reasonable values of electrical conductivity, σ, while the encapsulated atoms vibrate at a frequency that contributes to the scattering of phonons, which lowers the material's thermal

* Corresponding author. Fax: +1 530 752 8995.
E-mail address: smkauzlarich@ucdavis.edu (S.M. Kauzlarich).

0022-4596/$ - see front matter © 2011 Elsevier Inc. All rights reserved.
doi:10.1016/j.jssc.2011.02.027

conductivity, κ. There exists a rich literature of reports on thermoelectric properties of ternary type-I clathrates with the general formula $(2)_8(13)_x(14)_{46-x}$, where the numbers in parentheses indicate the appropriate group from the Periodic Table and the subscripts indicate stoichiometry. Fig. 1 offers a depiction of the type-I clathrate, space group $Pm\bar{3}n$, highlighting the two cages which act as building blocks for the structure. Group 13 and 14 elements occupy the 6*c*, 16*i* and 24*k* crystallographic sites, while group 2 elements occupy the 2*c* and 6*d* sites. One approach to optimize thermoelectric properties of a ternary type-I clathrate structure has been to adjust the ratio of group 13 to group 14 elements in order to obtain a Zintl phase with carrier concentration between 10^{19} and 10^{20} carriers/cm^3 [2,9]. Simple electron counting reveals a charge-balanced compositional stoichiometry to be $(2)_8(13)_{16}(14)_{30}$. Group 2 elements donate $16e^-$ that precisely fill the bonding orbitals of the group 13 and 14 framework atoms, and optimized thermoelectric compositions deviate only slightly from the charge-balanced composition.

Clathrates with an Al–Si framework have lower densities and higher melting points than their Ga–Ge counterparts, which make them candidates for high-temperature and weight-sensitive applications. The Al–Si type-I clathrate system is isostructural to the Ga–Ge system, but is often ignored as a high *zT* thermoelectric candidate because of its relatively higher thermal conductivity ($\sim$25 vs. 10 mW/cm K), and lower Seebeck values (~ -30 vs. -60 μV K^{-1}@ RT) [10,11]. Light elements in general are expected to provide higher lattice thermal conductivity values since their strong covalent bonds, along with their low mass lead to high phonon group velocity. This detrimental aspect of the covalent bonds in thermoelectric materials may be overcome with nanostructuring [2,12] to create additional phonon scattering points, allowing for a light-weight, high *zT* material. Therefore it is important to identify promising light-element containing materials.

Currently there is a great deal of research focused on clathrate structures with a Ga–Ge framework, because compounds with high *zT* values have been discovered within this system, such as $Ba_8Ga_{16}Ge_{30}$ [13,14] and $Ba_{24}Ga_xGe_{100-x}$ ($0 \le x \le 16$) [15]. These materials can display both n-type and p-type [9] transport properties, depending on their Ga:Ge ratio. To date, Ba–Ga–Ge type-I clathrates grown by the Czochralski method have reported *zT* values of 0.8 at 1050 K [16] and 1.35 at 900 K [13]. Slight deviations from the 16Ga:30Ge ratio have been shown to alter the thermoelectric properties [10,17]. These examples illustrate how composition of the sample is crucial in optimizing the material's thermoelectric properties. Ternary Ge and Si based clathrates, such as $Ba_8Ga_{16}Ge_{30}$ [13,14,16,18], $Sr_8Ga_{16}Ge_{30}$ [19,20] and $Ba_8Ga_{16}Si_{30}$ [18], have also been shown to be good thermoelectric materials; their study has promoted research into new quaternary systems, such as $Ba_8Ga_{16-x}In_xGe_{30}$ [21].

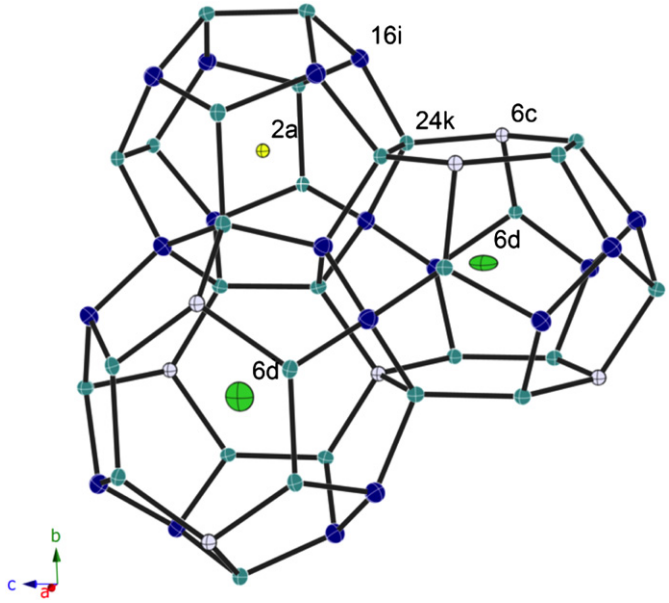

Fig. 1. Type-I clathrate structure showing the tetrakaidecahedra and smaller dodecahedron cages. Thermal ellipsoids represent the atomic sites according to their crystallographic notation.

Despite the discovery of high *zT* in Ga–Ge type-I clathrates, an isostructural Al–Si-based clathrate of comparable *zT* has yet to be reported. Theoretical studies have predicted the formation of the type-I clathrate $Ba_8Al_{16}Si_{30}$ to be thermodynamically favorable and, consistent with other type-I clathrates, predict $Ba_8Al_{16}Si_{30}$ to be a charge-balanced semiconductor [22]. To date, $Ba_8Al_xSi_{46-x}$ type-I clathrate samples have been aluminum deficient ($x < 16$), n-type, and exhibit metallic conductivity [7,11,23]. High-temperature thermoelectric properties have been measured on $Ba_8Al_{14}Si_{31}$ and $EuBa_7Al_{13}Si_{33}$ synthesized by direct methods; their high-temperature *zT* is promising, with a value of 0.35 for the Ba–Al–Si phase at 1000 °C [24]. Phase composition was determined for these samples by microprobe analysis, assuming the cation site to be fully occupied, as powder X-ray diffraction suggested a single-phase clathrate type-I structure. The $Ba_8Al_{14}Si_{31}$ phase made by Al flux has been structurally characterized, including single-crystal neutron diffraction measurements, MAS ^{27}Al NMR, and measurement of thermoelectric properties up to room temperature [11]. A combination of structure determination and density measurements led to the proposal that the cation site was filled and that the framework contained vacancies, consistent with published findings [7]. Single-crystal refinements with both cation and framework deficient composition $Ba_{7.5}Al_{13}Si_{29}$, as well as the Sr and Eu substituted phases, $Ba_{7.3}Sr_{0.7}Al_{14}Si_{31}$ and $Ba_{7.7}Eu_{0.3}Al_{14}Si_{31}$, prepared via Al flux synthesis have been reported [23,25]. For the latter two samples, the compositions were determined via wavelength dispersive microprobe analysis. They are consistent with framework occupancy trends reported for $Ba_8Al_xSi_{42-3/4x}\square_{4-1/4x}$ [7,26,27]. However, binary Si clathrates such as $K_{7.62}Si_{46}$ and $Rb_{6.15}Si_{46}$ follow a different trend: these clathrates are cation deficient [28] rather than framework deficient. Clathrates containing elements from period 4 and below, for example $Ba_8Ge_{43}\square_3$ and $Cs_8Sn_{44}\square_2$, have been shown to form vacancies in their framework [29,30]. The formation of vacancies has been attributed to the accommodation of the excess electrons donated from the cation. Instead of filling antibonding orbitals (conduction band), these electrons can fill nonbonding orbitals made available by the formation of vacancies (each vacancy requires $4e^-$) [9,29,31]. In the examples described above, the Seebeck coefficients are negative, suggesting that these clathrate phases are n-type and electron rich.

The report of varying Sr:Ba ratios in crystals of $(SrBa)_8(GaGe)_{46}$ produced from a Ga flux synthesis (discussed further below) [32], along with the uncertainties in composition described above (that is whether or not there are defects in the cation vs. framework sites [25,23]), provided an incentive for a detailed analysis of the Sr doped Ba–Al–Si clathrate phase produced from Al flux. Promising low-temperature thermoelectric properties [25] of the Sr doped clathrate produced via Al flux reaction that might translate into high-temperature high *zT* thermoelectric properties provided additional rationale for returning to this phase and to re-evaluate the structure. In addition, the high-temperature thermoelectric properties had not yet been determined.

We have studied a Sr doped clathrate, $Ba_{8-y}Sr_yAl_{14.2(2)}Si_{31.8(2)}$ ($0.77 < y < 1.3$), formed by Al flux synthesis and hot pressed into a pellet for high-temperature thermoelectric measurements. This

paper presents an analysis of structure and composition, and provides the high-temperature thermoelectric properties for this material. Single-crystal X-ray diffraction (90 and 12 K) and microprobe characterization indicate that the cation sites are nearly fully occupied (99%) and that there are no framework vacancies. Microprobe analysis indicates that the flux synthesis results in crystals with varying Sr incorporation, independent of Al content. High-temperature thermoelectric properties have been measured and the thermoelectric figure of merit (zT) is found to reach 0.3 at 1273 K.

2. Experimental procedure

2.1. Synthesis

The elements, Ba (Alfa Asear, 99.9%), Sr (Alfa Asear, 99%), Al (Sigma Aldrich, 99%) and Si (Alfa Asear, 99.9999%) were combined in an alumina crucible according to the stoichiometry 2Ba:2Sr:30Si:70Al, and sealed in a fused silica jacket under dynamic vacuum. Three samples were prepared in which the atomic ratios were scaled to 3 g of Al flux. No other ratios were investigated, as this was the optimal ratio for flux synthesis determined previously [25]. Samples were heated to 1000 °C and cooled slowly to 900 °C at 1 °C/h, followed by removal of excess aluminum flux by centrifugation. Each preparation yielded approximately 1.5 g of crystals, ranging from 3 to 8 mm cross section. A cooling rate of 2 °C/h yielded smaller crystals and a smaller yield. The crystals were washed with 2.5 M NaOH solution overnight to remove residual Al from their surface. Washed crystals were ground to a powder with a mortar and pestle. The powder was characterized by X-ray and microprobe analysis and hot pressed into pellets for thermoelectric property characterization. A fourth sample of single crystals was synthesized by the method described above and used for single crystal X-ray diffraction.

2.2. Thermoelectric properties sample preparation

To obtain a dense sample, approximately 3 g of the material was ground with a mortar and pestle into a powder and hot-pressed in a high-density graphite die (POCO). The hot-pressing was conducted at a pressure of about 20,000 psi at 1173 K for 1.3 h under an argon atmosphere. A dense cylinder several millimeters long and 12 mm in diameter was thus obtained. The density of the pellet (calculated from measured dimensions and weight) was found to be approximately 87% of the theoretical density of the pure clathrate phase.

2.3. Powder X-ray diffraction

Powder X-ray diffraction (PXRD) data were collected with a Bruker D8 Advance diffractometer employing Cu $K\alpha$ radiation, 40 KeV, 40 mA on the pressed pellet and single crystal samples that were ground into a powder. Data were collected on a rotating sample (15 rpm) from 10° to 80° (2θ), with a step size of 0.02399° and a step time of 1 s. Data acquisition was performed using the Bruker Command Center software. The Jade software program [33] was used to refine lattice parameters from the experimental data.

2.4. Microprobe characterization

The polycrystalline powder used for hot pressing and a slice of the hot-pressed pellet were both characterized by microprobe analysis. The samples were mounted and polished in epoxy and characterized with a Cameca SX-100 electron microprobe equipped with five wavelength dispersive spectrometers, operating at 10 nA current with a 10 kV accelerating potential and a beam diameter of approximately 1 μm. Multiple spot measurements were made across grains to obtain a representative composition of the sample. Elemental mapping was used to determine the homogeneity of each element over a large region of the sample. The standards $SrAl_2Si_2$, $BaAl_{3.54}Si_{0.41}$ (used for Ba and Al), and Si, were used to calculate elemental compositions. All totals were within 1% of 100% by weight, indicating that the only elements present in the samples are Ba, Sr, Al, and Si. Weight totals were converted to atomic % and normalized to 100% for nominal composition calculations.

Analysis of the composition: Atomic percentages from the electron microprobe analysis were imported into a spreadsheet and atomic % was normalized to the smallest elemental abundance, in this case strontium. Then, the ratios were multiplied by a constant to obtain values which would provide either full occupancy in the cation sites or full occupancy in the framework sites. This process was carried out for each individual data point for both the single crystal and pressed pellet samples. A macro was employed to streamline the process. The results are reported in Table 1.

2.5. Single crystal diffraction measurements

Single-crystal diffraction data were collected at 90 and 12 K using a Bruker Apex 2 CCD diffractometer, employing graphite-monochromatized Mo $K\alpha$ radiation (λ=0.71073 Å). The same crystal, mounting pin and data collection strategy were used for both data collections. For the 12 K data the instrument was equipped with a Cryo Industries of America CRYOCOOL LHe device. Before and after the data collection the temperature was measured with a calibrated Si diode placed at the crystal position. The SAINT program was used to correct for Lorentz and polarization corrections. Absorption corrections were made with the program SADABS [33]. A summary of the data collection details is given in Table 2.

Although the scattering factors for Al and Si are similar, there is no particular difficulty in distinguishing between the two elements by X-ray diffraction, so long as the atoms occupy distinct, separate positions. (example: $BaAl_2Si_2$ [34]). However, when there is mixed occupancy, the similarity of the scattering factors causes difficulties with the determination of occupancy ratios. To assist in the refinement of the present structure, the

Table 1
Microprobe compositions of the polycrystalline powder and models for the compositional stoichiometry.

Grain	Ba	Sr	Al	Si	C8 model composition	Framework total, C8 model	F46 model composition	Cation total, F46 model
1	13.19(10)	1.41(9)	26.47(12)	58.93(17)	$Ba_{7.23(5)}Sr_{0.77(5)}Al_{14.50(12)}Si_{32.29(30)}$	46.79(39)	$Ba_{7.10(6)}Sr_{0.76(5)}Al_{14.26(7)}Si_{31.74(7)}$	7.87(7)
2	12.13(10)	2.46(6)	26.31(9)	59.10(16)	$Ba_{6.65(3)}Sr_{1.35(3)}Al_{14.43(12)}Si_{32.41(33)}$	46.83(44)	$Ba_{6.53(6)}Sr_{1.33(3)}Al_{14.17(5)}Si_{31.83(5)}$	7.85(7)
3	13.07(12)	1.45(5)	26.54(14)	58.94(20)	$Ba_{7.20(3)}Sr_{0.80(3)}Al_{14.63(13)}Si_{32.47(37)}$	47.10(48)	$Ba_{7.03(7)}Sr_{0.78(3)}Al_{14.28(8)}Si_{31.72(8)}$	7.81(8)
4	12.49(8)	2.08(7)	26.40(13)	59.03(18)	$Ba_{6.86(4)}Sr_{1.14(4)}Al_{14.50(10)}Si_{32.41(28)}$	46.91(34)	$Ba_{6.73(5)}Sr_{1.12(4)}Al_{14.22(8)}Si_{31.78(8)}$	7.85(6)
5	12.25(11)	2.37(7)	26.32(10)	59.06(17)	$Ba_{6.70(4)}Sr_{1.40(4)}Al_{14.40(13)}Si_{32.31(34)}$	46.71(45)	$Ba_{6.60(7)}Sr_{1.28(4)}Al_{14.18(6)}Si_{31.82(6)}$	7.88(8)

Table 2
Crystallographic data and structure refinement parameters.

Temp (K)	90	12
Chemical formula[a]	$Ba_{7.37}Sr_{0.59}Al_{14.22}Si_{31.78}$	$Ba_{7.36}Sr_{0.60}Al_{14.24}Si_{31.75}$
Space group	*Pm*-3*n*	
Size (mm)	$0.123 \times 0.114 \times 0.088$	
a (Å)	10.6059(12)	10.6040(12)
V (Å^3)	1193.0(2) Å^3	1192.4(2) Å^3
Z	1	
Density (calcd) (Mg/m^3)[a]	3.24	3.24
Abs coeff (mm^{-1})	7.862	7.866
θ range	2.72–33.41°	2.72–33.13°
Reflns collected	7075	7054
Data/restraints/params	5951/1/21	5937/1/21
R (σ)	0.0340	0.0330
Final R indices [$I > 2\sigma(I)$]	$R_1 = 0.0233$ $wR_2 = 0.0441$	$R_1 = 0.0223$ $wR_2 = 0.0428$
Largest diff. peak and hole (fm Å^{-3})	0.27 and −0.32	0.33 and −0.38

[a] Determined from microprobe analysis.

average microprobe value of 14.22(5) Al atoms/unit cell was introduced as an additional observation with high weight. In addition, each Al/Si site was constrained to be fully occupied. Vacancies were allowed at the Ba(Sr) sites, in accordance with microprobe results. Individual occupancies were then allowed to vary. Both the 90 K and the 12 K data were refined in the same manner.

The uncertainties in the refined occupancies were reduced by a factor of two if equivalent intensities were not merged. Model calculations suggest that this is connected to the presence of systematic errors in the data. If a model set is constructed with no systematic errors, the effect on uncertainties is not seen. The results reported herein are based on unmerged data.

2.6. Thermoelectric properties measurements

Samples in the form of disks (typically slices 1 mm thick, 12 mm diameter) were cut from the pressed cylinder with a diamond saw. Such samples were used for measurements of electrical and thermal transport properties, while the Seebeck coefficient measurement was performed on the remaining cylinder. Measurements were performed in an inert atmosphere or under dynamic vacuum.

The electrical resistivity (ρ) was measured using the van der Pauw technique with a current of 100 mA, using a special high-temperature apparatus. The Hall coefficient was measured in the same apparatus, with a constant magnetic field value of about 10,000 G. The carrier density was calculated from the Hall coefficient, R_H, assuming a scattering factor of 1.0 in a single-carrier scheme, by $n = 1/R_H e$, where n is the density of free electrons and e the charge of the electron. The Hall mobility m_H was calculated from the Hall coefficient and the resistivity values with $m_H = R_H/\rho$.

At room temperature the Seebeck coefficient was measured with Copper-Constantan probes and above 400 K using a high-temperature light-pulse technique with Nb/W thermocouples.

The thermal diffusivity and heat capacity were estimated by laser flash technique in a Netzsch LFA 457 system up to 1000 °C in dynamic vacuum using a pyroceram standard for heat capacity measurements. The heat capacity was found to be close to the Dulong–Petit ($3k_b$/atom) value, with a slight, linear increase with temperature. Heat capacity and the experimental density were used to calculate the thermal conductivity from the thermal diffusivity measurements.

3. Results and discussion

3.1. Flux synthesis

In many studies flux synthesis has been used to prepare clathrate crystals [11,23,25,35–37]. Flux reactions can provide new routes to compositions and compounds that are difficult to prepare in high yield and as high quality crystals by direct synthesis methods [38–41]. Al has been used successfully as a reactive flux to prepare single crystals of binary and ternary Al–Si phases [38]. Single crystals of the Ba–Al–Si type-I clathrate structure were obtained via Al flux synthesis. In order to provide two different cations as guest ions, we have employed Sr in a flux reaction as described in the experimental section. Single crystals can be easily prepared; however, the amount of Sr incorporated into the structure was limited, ranging only from 0.78 to 1.33 atoms per unit cell (see below). The Sr incorporation may depend upon the cooling rate and temperature range before spinning off the Al flux. In a similar study, crystals of $(Ba/Sr)_8Ga_{16}Ge_{30}$ were grown in Ga flux by slowly cooling a mixture of the elements from 1100 to 700 °C at 3 °C/h [32]. EDX analysis confirmed the presence of $Sr_8Ga_{16}Ge_{30}$ and $Ba_8Ga_{16}Ge_{30}$ as well as phases containing mixtures of the two cations. However, in the Al–Si system, when reactions were prepared with Sr as the only group 2 element used in the starting composition and at the same temperatures employed (1000–900 °C at 1 °C/h), $SrAl_2Si_2$ is the predominant product [36].

3.1.1. Powder X-ray diffraction measurements

Fig. 2 shows the powder X-ray diffraction patterns of both the single crystals ground into powder and the hot pressed pellet samples. The diffraction patterns are consistent with type-I clathrate phase, with the exception of several small impurity peaks for $SrAl_2Si_2$, Si and Al that are indicated. The lattice parameters of the polycrystalline powder and the hot-pressed pellet were similar (10.6136 (1) Å for the polycrystalline powder; and 10.6126 (1) Å for the pressed pellet). These values are similar to that previously reported for $Ba_{7.3}Sr_{0.7}Al_{14}Si_{31}$ (10.6171 (5) Å) [25] but are slightly

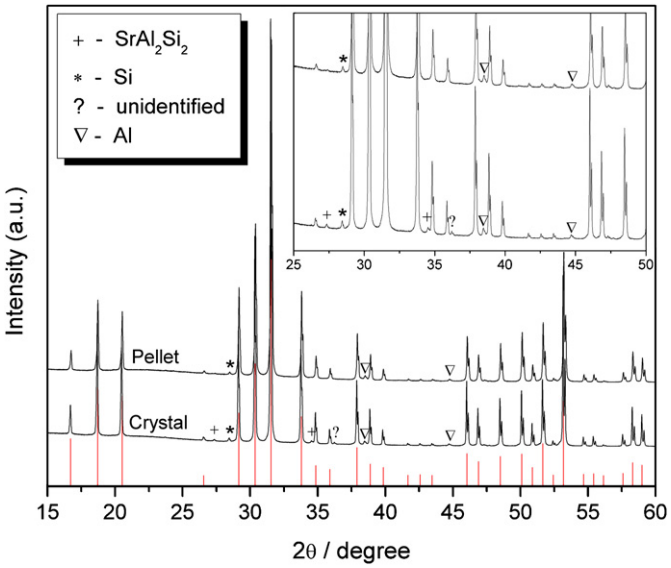

Fig. 2. X-ray powder diffraction pattern for $Ba_7Sr_1Al_{14}Si_{32}$. Experimental data for the pressed pellet and polycrystalline powder samples are shown along with the calculated diffraction pattern indicated as lines. The peaks marked with + correspond to the $SrAl_2Si_2$ phase, peaks marked with * for Si and peaks marked with a ∇ indicate Al.

smaller than the lattice parameter of 10.6246 Å reported for $Ba_8Al_{14}Si_{31}$ [11,24].

3.1.2. Microprobe analysis

Fig. 3 shows the back scattering electron (BSE) images of a typical grain used for the compositional analysis of the single crystals that were ground into powder and of the hot-pressed pellet sample. The contrast of the instrument had been set to distinguish the Sr and Ba content based on grain contrast. Two questions were considered in the determination of the compound compositional stoichiometry: whether or not the phase is framework deficient or cation deficient and whether or not the relative amounts of Ba and Sr are homogeneous throughout the sample.

Table 1 contains atomic % and nominal compositions calculated for the single crystals using a cation or a framework model as well as totals for framework and cation occupancy. To determine the composition, two models were employed: one with a general formula of 8 cation atoms (C8) and the other with 46 framework atoms (F46) per unit cell. Nominal compositions determined using the F46 model yielded cation occupancies slightly less than 8, while the C8 model yielded framework occupancies above 46 atoms per unit cell. Therefore, the most realistic model based on this analysis is with the framework fully occupied and the cation sites slightly deficient. The average nominal composition for the single crystals is $Ba_{6.8(3)}Sr_{1.1(3)}Al_{14.22(5)}Si_{31.78(5)}$ and the phase will be indicated as $Ba_7Sr_1Al_{14}Si_{32}$ hereafter. After establishing that the framework sites are fully occupied, the Sr and Al composition was scrutinized. Fig. 4 shows a plot of Sr vs. Al content, providing information about the amount of Sr incorporation with Al content in five grains measured. There are 3 (distinct by standard uncertainty, listed as atomic %) Sr compositions observed: ~1.3% (grains 2 and 4), ~1.9% (grain 5), and ~2.3% (grains 1 and 3). Distinct Sr incorporation suggests that during the synthesis crystals with a small range of Sr composition can be formed from the Al flux. In the five grains the Al content ranges from 26.7 to 27.5 at% and there is no correlation between Al and Sr content. It is worth noting that Sr and Ba are loaded in equal molar amounts into the reaction vessel; however, no crystals were grown with an equal incorporation of Sr and Ba or even a 2:6 ratio as might be favorable when considering the different sizes of the polyhedron cages in a type-I clathrate structure. Rather, only a small range of Sr is incorporated (0.78–1.33 atoms/unit cell) while the Al content is fairly consistent over the five grains measured, with the average Al atoms per unit cell equal to 14.22(5). This result suggests there is a competing synthetic process. Crystals of $SrAl_2Si_2$ ($CaAl_2Si_2$ structure type) have been prepared by Al flux under similar synthetic conditions [36], and small peaks matching this phase were observed in the PXRD patterns. It should also be noted that if a starting ratio of 8Ba:70Al:30Si is used with the same heating profiles reported in this study, only crystals of $BaAl_2Si_2$ are formed.

In order to determine whether or not the composition changes upon hot-pressing, microprobe analysis of a slice of the hot-pressed pellet was performed. Similar to the polycrystalline powder sample, compositions calculated using the C8 model yielded frameworks with more than 46 framework atoms per unit cell, while the F46 model yielded vacancies on the cation site. The average nominal composition was $Ba_{6.77(2)}Sr_{1.02(2)}Al_{14.18(3)}Si_{31.82(3)}$ using the framework model, within the uncertainty of the single crystal composition, in good agreement with the sample before hot pressing. Atomic percentages, nominal compositions and total occupancies of framework and cation models are listed in Supplementary Table S1.

Elemental mapping of Ba, Sr, Al and Si (Fig. 5) was used to analyze the overall sample uniformity; many grains can be assessed simultaneously using this technique. Small regions of elevated Al and Si content are consistent with the PXRD pattern from the pressed pellet. Peaks from the $SrAl_2Si_2$ phase can be

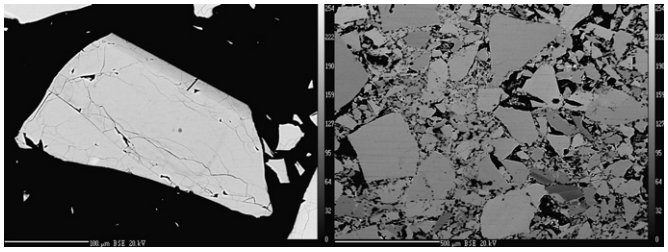

Fig. 3. (a) BSEI of a typical single grain of the polycrystalline powder used in hot pressing. 30 data points along the length of the grain were collected and used to determine the nominal composition of the polycrystalline powder. (b) BSEI image of the pressed pellet.

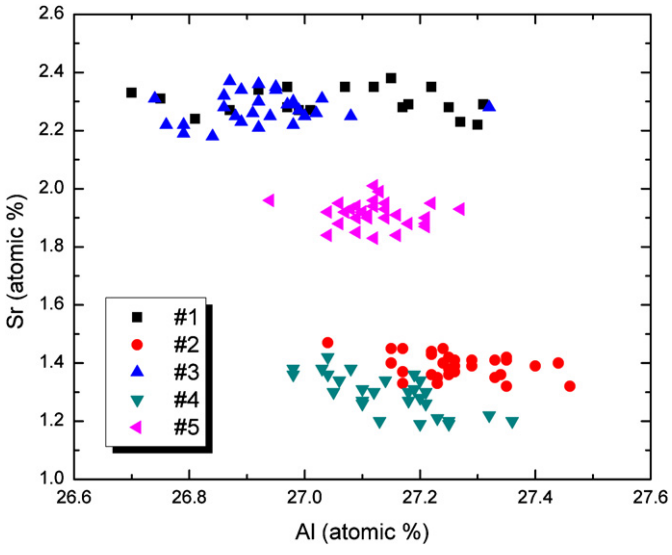

Fig. 4. Sr and Al content by atomic % for grains measured by microprobe analysis in the polycrystalline powder sample. While the range of Al content is well distributed in all the grains, the Sr content is distinctive for each grain.

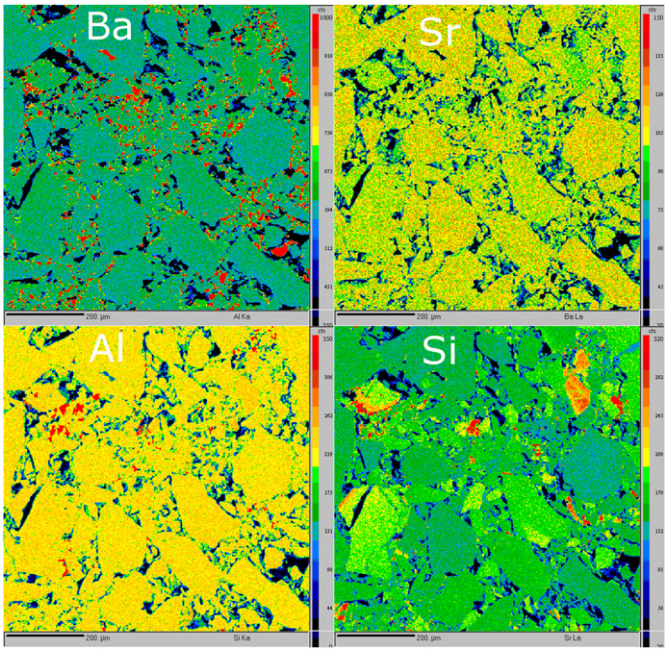

Fig. 5. X-ray elemental mapping of Ba, Sr Al and Si on the surface of the pressed pellet sample. The scale bar is 200 μm.

identified in the PXRD pattern of the polycrystalline powder, but not in the pressed pellet. The enriched Sr content in the upper right corner of the Sr elemental map is likely from an amorphous Sr phase formed during the pressing of the $SrAl_2Si_2$ phase. In general, the elemental maps appear to be mostly homogeneous, with a few regions of different intensity. The agreement between compositions of the clathrate phases before and after pressing indicate that the observed impurity phases are intrinsic to this synthetic method and not obtained via decomposition during the pressing process.

3.1.3. Single crystal diffraction

Previous X-ray and neutron work on single-crystal refinements of Al–Si based type-I clathrates have been unable to determine specific site occupancies of Al on framework sites, Wyckoff symbols 6*c*, 16*i* and 24*k* [11,25], due to the quality of the data sets and specifics of the refinement. The refinement of Al–Si content on mixed occupancy sites is unreliable in structures with large atomic displacement parameters (ADPs) and partial site vacancies. This leads to an increased uncertainty in the local electron count and thereby understanding of the transport properties. In situations where all sites are fully occupied and there is no mixed occupancy, low-temperature X-ray diffraction can establish the positions of Al and Si atoms [34]. In this study, low temperature X-ray diffraction at 90 and 12 K is employed. The lowest temperature was expected to reduce ADPs sufficiently to reach conclusions about site occupancies and vacancies. However, we note that the ADPs at 12 K are larger than would ideally be expected. It is likely that this is caused by inexact atomic positions, i.e. in reality, Al and Si atoms do not occupy exactly the same positions. Indeed, split site positions have been observed in the clathrate $K_7B_7Si_{39}$ [42] and in some inverse clathrate structures [43,44], where a greater contrast in scattering factors makes it possible to distinguish the split sites at room temperature.

A preliminary refinement was first attempted where the Al/Si ratios on each framework site were allowed to independently refine; this resulted in an Al content of ~9 atoms and ~13 atoms per unit cell for the 90 and 12 K data, respectively. In particular, the results for the 90 K data were deemed unsatisfactory, because the refined composition did not match the Al content from the microprobe data. We note that the composition obtained from the 12 K data is not seriously different from the microprobe results. Next, the total Al content was restrained to the average

Table 3
Refined site occupancies, atoms per unit cell and equivalent isotropic displacement parameters at 90 and 12 K.

Site		Site occupancy *atoms per unit cell*[*]		U_{eq} (Å^2)[a]	
		90 K	12 K	90 K	12 K
Cation, 2*a*	Ba	0.703(3) *1.406*(6)	0.700(3) *1.400*(6) *1.289*(5)	0.00563(6)	0.00422(6)
	Sr	0.297(3) *0.594*(6)	0.300(3) *0.600*(6) *0.710*(5)	0.00563(6)	0.00422(6)
Cation, 6*d*	Ba	0.9943(9) 5.966(5)	0.9936(9) 5.962(5) *5.79*	0.01806(4)	0.01398(4)
Framework, 24*k*	Al	0.345(7) *8.28*(16)	0.357(7) *8.56*(17) *9.15*(17)	0.00698(7)	0.00621(7)
	Si	0.655(7) *15.72*(16)	0.643(7) *15.44*(17) *14.85*(17)	0.00698(7)	0.00621(7)
Framework, 16*i*	Al	0.135(15) *2.16*(24)	0.074(15) *1.18*(24) *0.94*(28)	0.00893(10)	0.00848(10)
	Si	0.865(15) *13.84*(24)	0.926(15) *14.82*(24) *15.05*(28)	0.00893(10)	0.00848(10)
Framework, 6*c*	Al	0.63(4) *3.76*(23)	0.75(4) *4.48*(24) *4.13*(26)	0.0069(2)	0.0057(2)
	Si	0.37(4) *2.24*(23)	0.25(4) *1.52*(24) *1.87*(26)	0.0069(2)	0.0057(2)

[*] Atoms per unit cell—product of the site occupancy and the Wykoff site multiplicity.
[a] U_{eq} is defined as one-third of the trace of the orthogonalized U^{ij} tensor. For the 2*a* site all tensors were equivalent (Isotropic displacement).

Table 4
Bond lengths (Å) and angles (deg) at 12 and 90 K.

	Bond lengths (Å)			Bond angles (deg)	
	12 K	90 K		12 K	90 K
2*a*–16*i*	3.3964(3)	3.3972(5)	16*i*–24*k*–6*c*	105.49(1)	105.49(1)
2*a*–24*k*	3.4693(3)	3.4696(5)	16*i*–24*k*–16*i*	106.54(1)	106.57(1)
6*d*–6*c*	3.7491(1)	3.7498(4)	16*i*–24*k*–24*k*	106.99(1)	106.98(1)
6*d*–24*k*	3.5835(2)	3.5847(4)	16*i*–16*i*–24*k*	109.27(1)	109.28(1)
16*i*–16*i*	2.3905(6) 2.3900(7)	2.3906(7)	24*k*–16*i*–24*k*	109.67(1)	109.66(1)
16*i*–24*k*	2.4467(2) 2.4468(2)	2.4468(3)	24*k*–6*c*–24*k*	108.46(1)	108.44(1)
24*k*–24*k*	2.4923(5) 2.4926(5)	2.4938(6)	24*k*–6*c*–24*k*	111.52(1)	111.56(1)
6*c*–24*k*	2.4969(3) 2.4968(3)	2.4975(4)	6*c*–24*k*–24*k*	124.24(1)	124.22(1)

microprobe composition obtained for the single crystals (Al=14.22 (5)), and individual site occupancies were allowed to refine; this resulted in a stable refinement. The final refinement parameters for the 90 and 12 K data are summarized in Table 2, occupancies and equivalent isotropic displacement parameters in Table 3, and bond lengths and angles are provided in Table 4. Because the Al content is set by the microprobe data in both refinements, the final compositions are almost identical. However, the Al–Si site occupancies for the 6*c* and 16*i* sites (discussed below) are slightly different between the two data sets. For the sake of simplicity, the 12 K data will be highlighted when discussing site occupancies that are similar between the two data sets.

The 2*a* site (small cage) is fully occupied and contains both Sr and Ba. The Sr content is 0.600(6) Sr atoms per unit cell, below the observed range found in the microprobe analysis (0.77–1.33 atoms/unit cell). It is likely that individual crystals have different Sr incorporation, as illustrated by the observed range found by microprobe. The Sr content of the single crystal chosen for X-ray diffraction is lower than the range observed by microprobe, indicating that less Sr is possible and that the maximum solubility is 1.33 atoms/unit cell. The 6*d* site (large cage) is 99% occupied by Ba; it is modeled with anisotropic ADPs. For the type-I clathrates, $Eu_8Ga_{16}Ge_{30}$, $Ba_8Ga_{16}Sn_{30}$, $Sr_8Ga_{16}Ge_{30}$ and $Ba_8Al_{16}Ge_{30}$, the atom in the large cage can be refined with split-site model (24*k*/24*j* positions), rather than the central 6*d* position [4,45]. In this study, the resolution of the data does not permit a split-site refinement. Analysis of the microprobe data also suggests a cation vacancy of ~1%. Forcing the 6*d* site to full occupancy results in insignificant changes to agreement factors compared to the vacancy model, and in a small shift in Al/Si ratios on the framework sites. Because of the cation vacancy observed in the microprobe data, the occupancy of the site was allowed to freely vary during the refinement process; it remained stable at 99% occupancy.

For both the 90 and 12 K data sets the refined Al contents on the 24*k* site are statistically indistinguishable, ~8.5 Al atoms per unit cell. However, the data sets differ slightly in refined Al content on the 6*c* and 16*i* sites. The 90 K set favors Al content on the 16*i* site, 2.16(24) vs. 1.18(24), while the 12 K set favors Al content on the 6*c* site, 4.47(23) vs. 3.75(23). The difference between results from the two data sets is $\sim 4\sigma$. It is a safe assumption that the composition does not change with temperature for this crystal, therefore the changes in Al/Si occupancy on these sites can be attributed to differences between the data sets, and to changes in ADPs. In summary, the 6*c*, 24*k*, and 16*i* framework sites all contain a mixture of Al and Si and the site preference for Al is similar to that in other ternary type-I clathrates: $6c > 24k > 16i$. The site preferences are discussed further below.

It is instructive to examine the ADPs for Al(Si) in this clathrate. From the 90 K data set the average U_{eq} is 0.00760 Å^2. The corresponding value from the 12 K data set is 0.00680 Å^2. The ratio of the two values is 1.12. For comparison, the average Al and Si ADP values for the compound $BaAl_2Si_2$ are 0.00455 Å^2 at 90 K and 0.00358 Å^2 at 10 K [34]. The ratio is 1.27. $BaAl_2Si_2$ does not show signs of mixed occupancies or of other type disorder, and can therefore be used as a template. We assume that the higher ADP values and their relatively lower decrease with temperature indicate positional inaccuracy. Because the various interatomic distances are different, the Al and Si atoms that nominally occupy the same positions are assumed to occupy slightly different positions, and these positions do not exactly coincide with the various Wyckoff positions. The result is an apparent increase in ADP values and a decreased response to lowering of the temperature. Lowering the temperature cannot be expected to decrease the disorder inherent in this model, and will not result in a normal lowering of ADPs.

Table 4 provides selected bond lengths and angles. The refined site occupancies are reflected in the apparent bond lengths between the framework atoms. Al–Al bonds are expected to be the weakest and therefore longest, while Si–Si bonds are expected to be the strongest and shortest. For the refinement of the 12 K data set, the shortest bond lengths are between the 16*i* sites, 2.3905(7) Å (where the amount of Si is greater than Al). The distances between crystallographic sites increase with increasing Al occupancy: 16*i*–24*k* distance is 2.4468(3) Å, followed by the 24*k*–24*k* distance of 2.4921(6) Å and finally the 6*c*–24*k* distance of 2.4970(4) Å. The same trends are observed in the 90 K data set. These trends in bond length can also be observed in other type-I group 13–14 clathrates [11,35] and are consistent with the preference of the trivalent atom on the 6*c* site. The Ba_8Si_{46} type-I clathrate has been prepared by high pressure synthesis, and shows a different trend in bond lengths. In this system, the 24*k*–24*k* bond is the longest followed by the 24*k*–6*c* (2.477 and 2.415 Å) [46]. If Al was proportionally distributed onto each framework site, in other words, each site contains ~30% Al (14.2 Al atoms/46 framework atoms=30%), then the trend in bond lengths found for Ba_8Si_{46} would hold for the $Ba_7Sr_1Al_{14}Si_{32}$ system. However, since the bond length trend is modified in $Ba_7Sr_1Al_{14}Si_{32}$, the resulting refinement of Al on framework sites is supported.

Most reports suggest that trivalent atoms will be shared between all three framework sites in a manner which reduces energetically unfavorable bonding between them: unfavorable presumably because of the general trend in lower bond enthalpies of the group 13 over group 14 atoms. Recently efforts have been made, using crystallography, theory, ^{27}Al NMR and X-ray absorption fine structure (EXFAS) studies, to determine the individual site occupancies of the trivalent atoms in $(2)_8(13)_{16}(14)_{30}$ clathrates; in these studies Ba–Ga–Si, Ba–Al–Ge, and Ba–Ga–Sn were used as model system [11,45,47–49]. Table 5 lists the findings from these studies and the results from the 90 K data set.

All of the above studies are in agreement that the 6*c* site has greater than 50% occupancy of the group 13 atom; differences lie in the distribution of the remaining group 13 atoms on the 16*i* and 24*k* sites. Based on X-ray and neutron diffraction, a set of site occupancy rules for the total avoidance of group 13–13 bonds in the Ba–Al–Ge system has been suggested [45]. For the avoidance of group 13–13 bonds, two rules which pair site occupancies were developed: $Al(6c)+Al(24k) \leq 100\%$ and $Al(16i)+Al(24k) \leq 50\%$. First-principle calculations on Ba–Al–Ge have also been employed to determine the total energy of these structures with different site occupancy configurations [47]. In agreement with the site occupancy rules, the Al occupancy in the lowest energy configuration is calculated to be 50% for the 6*c* site, 6.25% for the 16*i* site and 50% for the 24*k* site. ^{27}Al NMR and ab initio calculations have been employed in conjunction to determine site occupancies [50].

Table 5
Comparison of site occupancy for the trivalent atom in the ternary type- clathrates with group 13/14 framework atoms.

Compound	6*c*	16*i*	24*k*
$Ba_8Ga_{14.6}Si_{31.4}$[a]	0.65	0.08	0.39
$Ba_7Sr_1Al_{14}Si_{32}$[b]	0.63	0.14	0.35
$Ba_8Al_{16.7}Ge_{29.3}$[c]	0.56	0.24	0.40
$Ba_8Ga_{16}Sn_{30}$[d]	0.71	0.36	0.25

[a] Ref. [49], synchrotron powder diffraction.
[b] This work, 90 K data.
[c] Ref. [45], single crystal X-ray diffraction.
[d] Ref. [48], single crystal X-ray diffraction.

Table 6
Bond enthalpies and differences[a].

Diatomic bond	kJ mol^{-1}	ΔEnthalpy	kJ mol^{-1}
Ga–Ga	106	ΔGaSi	204
Al–Al	133	ΔAlSi	177
Sn–Sn	187	ΔAlGe	131
Ge–Ge	264	ΔGaSn	81
Si–Si	310	ΔAlSn	54

[a] Luo, Y.-R. Comprehensive Handbook of Chemical Bond Energies, CRC Press: Boca Raton, 2007.

These results indicated that Al occupancies of 50%, 25%, and 34% (6*c*, 16*i* and 24, respectively) fit the experimental data best, although this configuration contains 2 trivalent bonds and did not have the lowest energy configuration. Neutron and synchrotron powder diffraction on Ba–Ga–Si also show that these rules are bent, resulting in Ga(6*c*)+Ga(24*k*)=104%. Most recently, X-ray diffraction [4] at 300 K was used with the Ba–Ga–Sn system to calculate site occupancies and to determine the number of Ga–Ga bonds. The trivalent atom is also determined to be the majority atom on the 6*c* site, but a larger fraction of trivalent atoms is found on the 16*i* sites compared to the Ba–Ga–Si and Ba–Al–Ge systems (36% vs. 24% vs. 8%). Here a different site occupancy rule is broken: 16*i*+24*k*=61%. Additional characterization with EXAFS confirms the 4–5 Ga–Ga bonds per unit cell in this system [11], in line with the breaking of the site occupancy rules. These examples give evidence that the minimization of group 13–13 bonds is not the only contributing factor to the formation these clathrates, other factors such as bond length and enthalpy warrant consideration.

Table 6 lists the bond enthalpies of the five framework atoms and their differences, a general trend can be observed across the four systems: presence of group 13 atoms in the 16i site decreases with increasing difference in bond enthalpy between the group 13 and 14 atoms. In the Ba–Ga–Si system, the 16*i* site has the smallest percentage of group 13 atoms; this system also has the largest difference in bond enthalpy. The Ba–Al–Si and the Ba–Al–Ge systems fit in between these two in terms of differences in bond enthalpies and occupancy of group 13 atom on the 16*i* site. The Ba–Ga–Sn system has the smallest difference in bond enthalpy and the largest percentage of group 13 atoms on the 16*i* site. The occupation of the 16*i* site by group 13 atoms has recently been linked to splitting of the cation at the 6*d* site and the occurrence of glass like thermal conductivity [51]. No reports of a Ba–Al–Sn clathrate have been published to date; if this system is thermodynamically stable it should have highest occupancy of group 13 atoms on the 16*i* site and glass-like thermal conductivity.

Overall, the compound produced by the flux synthesis shows no defects on the framework. Therefore, according to the stoichiometry of $Ba_7Sr_1Al_{14}Si_{32}$, we would expect metallic behavior. The composition determined from microprobe and the structural solution are in good agreement for Al occupancies, consistent with bond enthalpies, $6c > 24k > 16i$, for the three crystallographic sites.

3.2. Thermoelectric properties

Consistent with previously reported low-temperature data, $Ba_7Sr_1Al_{14}Si_{32}$ shows n-type conductance with a negative Seebeck coefficient and the resistance increases with increasing temperature, characteristic of metallic behavior (Fig. 6). The room-temperature resistivity of the pressed pellet sample is ~0.6 mΩ cm, while the resistivity of a single-crystal sample of similar composition, $Ba_{7.3}Sr_{0.7}Al_{14}Si_{31}$ was reported to be ~1.4 mΩ cm [11].

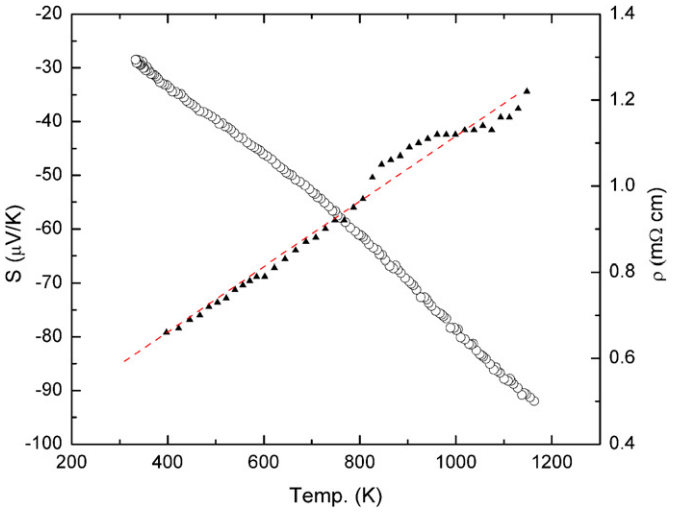

Fig. 6. Transport properties of $Ba_7Sr_1Al_{16}Si_{30}$. Open circles are Seebeck and black triangles are resistivity data. The linear fit of resistivity (red dashed line) was used to calculate *zT* (Fig. 7).(For interpretation of the references to color in this figure legend, the reader is referred to the web version of this article.)

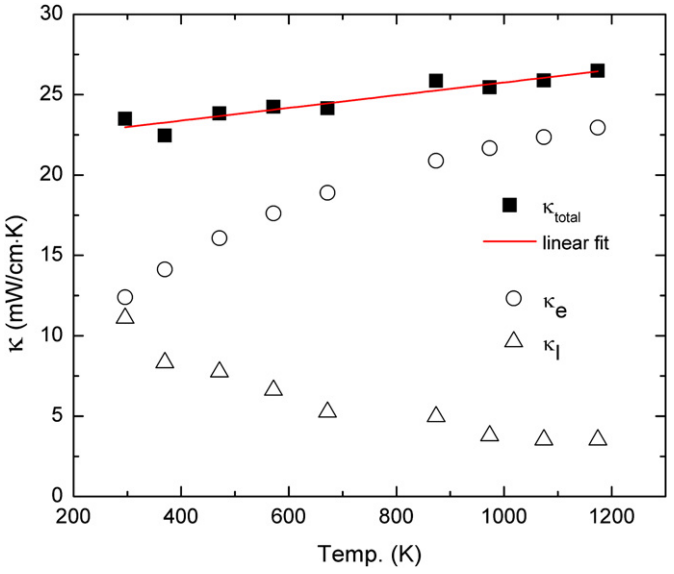

Fig. 7. Thermal conductivity, κ (mW/cm K) (black filled squares), electronic contribution (circles) and lattice contribution (triangles). The linear fit of κ_T (red dashed line) was used to calculate *zT* in Fig. 7. (For interpretation of the references to color in this figure legend, the reader is referred to the web version of this article.).

We would expect that a pressed pellet would have a higher resistance, because of the increased number of grain boundaries between crystallites. However in this case, the difference may be accounted for by the presence of metallic phases as observed in elemental maps (Fig. 5). While differences in carrier concentration could explain this difference in resistivity, the room-temperature Seebeck coefficients differ by less than 5 μV/K. The absolute value of the Seebeck coefficient changes from −29 μV/K at 333 K to −92 μV/K at 1168 K. Similar room-temperature Seebeck values of −21 and −32 μV/K have been reported for $Ba_8Al_{14}Si_{31}$ and $Ba_{7.3}Sr_{0.3}Al_{14}Si_{31}$, respectively [11,25]. Room-temperature Seebeck values of ~−48 μV/K for a $Ba_8Al_{16}Si_{30}$ sample made by arc welding [7], and −35 μV/K for the direct reaction synthesis product [24] have been reported.

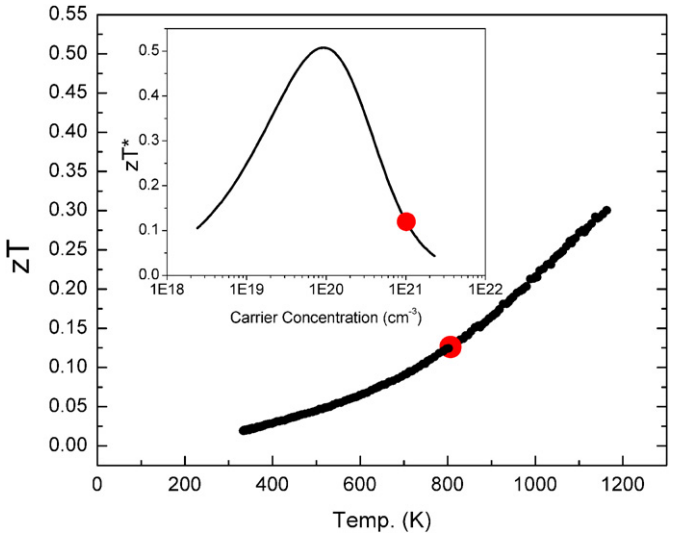

Fig. 8. Temperature dependence of the figure of merit, zT. Inset: single parabolic band model showing predicted zT^* with carrier concentration extrapolated from experimental parameters (larger circle indicated) at 800 K. If carrier concentration can be reduced to near 10^{20} cm^{-3} then an almost 5-fold increase in the figure of merit zT may be observed.

High-temperature measurements of the resistivity and Seebeck coefficient reveal linear behavior with temperature, consistent with the understanding of $Ba_7Sr_1Al_{14}Si_{32}$ as a heavily doped n-type semiconductor. As the Seebeck coefficient never exceeds -100 μV/K, there is clearly a need to prepare compositions closer to the charge-balanced state. The metallic behavior suggests the free-electron value of the Lorenz number of 2.4×10^{-8} J K^{-2} C^{-2} is appropriate. Application of this coefficient and the electronic conductivity in the Wiedemann–Franz law yields the lattice component of the thermal conductivity (Fig. 7). A clear decrease in the lattice component is observed with increasing temperature, as expected from phonon–phonon scattering.

The addition of Sr to this structure does not appreciably decrease its thermal conductivity [5], most likely because the Sr atom only occupies the crystallographic 2*a* site which does not allow for large ADPs. At high temperatures, the lattice thermal conductivity is quite low (3 mW/cm K at 1200 K), similar to $Ba_8Al_{14}Si_{31}$ [24]. With such a large electronic thermal conductivity term, it is difficult to determine if the mass contrast on the 2*a* site impacts the thermal conductivity. The thermoelectric figure of merit, shown in Fig. 8, attains a value of ~0.3 at 1200 K. With such a low lattice thermal conductivity value, we anticipate the potential for good thermoelectric performance if the carrier concentration could be sufficiently optimized.

To evaluate the potential magnitude of this improvement, the performance of $Ba_7Sr_1Al_xSi_{46-x}$ has been modeled using a single parabolic band model with the assumption of acoustic phonon scattering dominating transport at these high temperatures [10]. Transport values at 800 K ($S=66$ μV/K, $\rho=0.98$ mΩ cm) were used as input parameters with an estimated carrier concentration of 10^{21} cm^{-3} and $\kappa_l=\sim5$ mW/cm/K. Here the Seebeck coefficient is used to calculate the chemical potential for this sample. With the chemical potential and the above parameters in hand, the Lorenz number (L), effective mass and intrinsic mobility can be determined. Within this single parabolic band assumption, an estimate of zT can be calculated across a range of chemical potentials (and thus carrier concentrations), as shown in Fig. 7. A five-fold improvement in thermoelectric performance was estimated if the carrier concentration could be sufficiently reduced. Note that the peak zT in this model is rather insensitive to the magnitude of the high-temperature carrier concentration, which is the least certain input parameter for this model.

4. Summary

The type-I structured clathrate phase $Ba_{7.4}Sr_{0.6}Al_{14}Si_{32}$ has been synthesized by aluminum flux. Characterization by microprobe and single crystal X-ray diffraction analyses indicate that the structure has no framework vacancies and the cation sites are close to full occupancy (~99%). Microprobe analysis of single crystal grains prior to hot pressing indicate a range of Sr incorporation between 0.76 and 1.33 atoms per unit cell. A plot of Sr vs. Al content (atomic %) reveals that the incorporation of Sr is independent of the amount of Al, suggesting that in this system it is not necessary to shrink the dodecahedron cage to accommodate smaller cations. Single-crystal refinement in combination with compositions provided by microprobe analysis was able to determine site occupancies at 12 and 90 K. These site occupancies follow an expected trend based on bond enthalpies. Thermoelectric properties indicate n-type conductivity with a maximum zT of 0.3 at 1200 K. At 800 K carrier concentration is high, while the lattice thermal conductivity remains low (~5 mW/cm K). If a more charge balanced state between Ba, Sr and Al atoms can be achieved, the figure of merit, zT, is expected to be increased ~5-fold. It may be possible to tune carrier concentration through alkaline-earth/alkali metal ratio, such as Ba/K, in order to achieve a high zT material. Additionally, nanostructuring to reduce the overall lattice thermal conductivity would provide for further optimization.

Acknowledgments

We gratefully acknowledge the financial support from NSF DMR0600742 and NASA Jet Propulsion Laboratory. We thank Cathie Condron for her early contributions to the research.

Appendix A. Supplementary Information

Supplementary data associated with this article can be found in the online version at doi:10.1016/j.jssc.2011.02.027.

References

[1] J.R. Sootsman, D.Y. Chung, M.G. Kanatzidis, Angew. Chem. Int. Ed. 48 (2009) 8616–8639.
[2] G.J. Snyder, E.S. Toberer, Nat. Mater. 7 (2) (2008) 105–114.
[3] K. Suekuni, T. Tanaka, S. Yamamoto, M.A. Avila, K. Umeo, Y. Takasu, T. Hasegawa, N. Ogita, M. Udagawa, T. Takabatake, J. Electron. Mater. 38 (7) (2009) 1516–1520.
[4] M.A. Avila, K. Suekuni, K. Umeo, H. Fukuoka, S. Yamanaka, T. Takabatake, Appl. Phys. Lett. 92 (4) (2008) 041901.
[5] M. Christensen, S. Johnsen, B.B. Iversen, Dalton Trans. 39 (4) (2010) 978–992.
[6] M.M. Koza, M.R. Johnson, R. Viennois, H. Mutka, L. Girard, D. Ravot, Nat. Mater. 7 (10) (2008) 805–810.
[7] Y. Mudryk, P. Rogl, C. Paul, S. Berger, E. Bauer, G. Hilscher, C. Godart, H. Noel, J. Phys.—Condens. Matter. 14 (34) (2002) 7991–8004.
[8] M. Beekman, G.S. Nolas, J. Mater. Chem. 18 (8) (2008) 842–851.
[9] E.S. Toberer, A.F. May, G.J. Snyder, Chem. Mater. 22 (3) (2010) 624–634.
[10] A.F. May, E.S. Toberer, A. Saramat, G.J. Snyder, Phys. Rev. B 80 (12) (2009) 125205.
[11] C.L. Condron, J. Martin, G.S. Nolas, P.M.B. Piccoli, A.J. Schultz, S.M. Kauzlarich, Inorg. Chem. 45 (23) (2006) 9381–9386.
[12] A.J. Minnich, M.S. Dresselhaus, Z.F. Ren, G. Chen, Energy Environ. Sci. 2 (5) (2009) 466–479.
[13] A. Saramat, G. Svensson, A.E.C. Palmqvist, C. Stiewe, E. Mueller, D. Platzek, S.G.K. Williams, D.M. Rowe, J.D. Bryan, G.D. Stucky, J. Appl. Phys. 99 (2) (2006) 023708.

[14] A. Saramat, E.S. Toberer, A.F. May, G.J. Snyder, J. Electron. Mater. 38 (7) (2009) 1423–1426.
[15] J.H. Kim, N.L. Okamoto, K. Kishida, K. Tanaka, H. Inui, Acta Mater. 54 (8) (2006) 2057–2062.
[16] E.S. Toberer, M. Christensen, B.B. Iversen, G.J. Snyder, Phys. Rev. B 77 (7) (2008) 075203.
[17] J.D. Bryan, N.P. Blake, H. Metiu, G.D. Stucky, B.B. Iversen, R.D. Poulsen, A. Bentien, J. Appl. Phys. 92 (12) (2002) 7281–7290.
[18] N.P. Blake, D. Bryan, S. Latturner, L. Mollnitz, G.D. Stucky, H. Metiu, J. Chem. Phys. 114 (22) (2001) 10063–10074.
[19] V.L. Kuznetsov, L.A. Kuznetsova, A.E. Kaliazin, D.M. Rowe, J. Appl. Phys. 87 (11) (2000) 7871–7875.
[20] S.B. Schujman, G.S. Nolas, R.A. Young, C. Lind, A.P. Wilkinson, G.A. Slack, R. Patschke, M.G. Kanatzidis, M. Ulutagay, S.J. Hwu, J. Appl. Phys. 87 (3) (2000) 1529–1533.
[21] N.L. Okamoto, K. Kishida, K. Tanaka, H. Inui, J. Appl. Phys. 101 (11) (2007) 113525.
[22] E.N. Nenghabi, C.W. Myles, J. Phys.—Condens. Matter 20 (41) (2008) 415214.
[23] C.L. Condron, R. Porter, T. Guo, S.M. Kauzlarich, Inorg. Chem. 44 (25) (2005) 9185–9191.
[24] C.L. Condron, S.M. Kauzlarich, F. Gascoin, G.J. Snyder, Chem. Mater. 18 (20) (2006) 4939–4945.
[25] C.L. Condron, S.M. Kauzlarich, Inorg. Chem. 46 (7) (2007) 2556–2562.
[26] Y. Mudryk, P. Rogl, C. Paul, S. Berger, E. Bauer, G. Hilscher, C. Godart, H. Noel, A. Saccone, R. Ferro, Physica B 328 (1-2) (2003) 44–48.
[27] B. Kuhl, A. Czybulka, H.U. Schuster, Z. Anorg. Allg. Chem. 621 (1) (1995) 1–6.
[28] G.K. Ramachandran, P.F. McMillan, J. Solid State Chem. 154 (2) (2000) 626–634.
[29] W. Carrillo-Cabrera, S. Budnyk, I. Prots, Y. Grin, Z. Anorg. Allg. Chem. 630 (630) (2004) 2267–2276.
[30] A. Kaltzoglou, S.D. Hoffmann, T.F. Fassler, Eur. J. Inorg. Chem. 26 (2007) 4162–4167.
[31] H. Shimizu, T. Iitaka, T. Fukushima, T. Kume, S. Sasaki, N. Sata, Y. Ohishi, H. Fukuoka, S. Yamanaka, J. Appl. Phys. 101 (6) 63549-1-7.
[32] K.F. Cai, L.C. Zhang, Q. Lei, E. Müller, C. Stiewe, Cryst. Growth Des. 6 (8) (2006) 1797–1800.
[33] G.M. Sheldrick, XRD Single-Crystal Software, Bruker AXS, Madison, WI, 1999.
[34] C.L. Condron, H. Hope, P.M.B. Piccoli, A.J. Schultz, S.M. Kauzlarich, Inorg. Chem. 46 (11) (2007) 4523–4529.
[35] S.E. Latturner, J.D. Bryan, N. Blake, H. Metiu, G.D. Stucky, Inorg. Chem. 41 (15) (2002) 3956–3961.
[36] S.M. Kauzlarich, C.L. Condron, J.K. Wassei, T. Ikeda, G.J. Snyder, J. Solid State Chem. 182 (2) (2009) 240–245.
[37] J.D. Bryan, G.D. Stucky, Chem. Mater. 13 (2) (2001) 253–257.
[38] M.G. Kanatzidis, R. Pottgen, W. Jeitschko, Angew. Chem. Int. Edit. 44 (43) (2005) 6996–7023.
[39] J.L. Mathieu, S.E. Latturner, Chem Commun. 33 (2009) 4965–4967.
[40] M. Stojanovic, S.E. Latturner, J. Solid State Chem. 182 (8) (2009) 2239–2245.
[41] P.C. Canfield, Z. Fisk, Philosophical Mag. B—Phys. Condens. Matter Statistical Mechan. Electron. Opt. Magn. Properties 65 (6) (1992) 1117–1123.
[42] W. Jung, J. Loerincz, R. Ramlau, H. Borrmann, Y. Prots, F. Haarniann, W. Schnelle, U. Burkhardt, M. Baitinger, Y. Grin, Angew. Chem. Int. Edit. 46 (35) (2007) 6725–6728.
[43] K.A. Kovnir, A.V. Sobolev, I.A. Presniakov, O.I. Lebedev, G. Van Tendeloo, W. Schnelle, Y. Grin, A.V. Shevelkov, Inorg. Chem. 44 (24) (2005) 8786–8793.
[44] K.A. Kovnir, M.M. Shatruk, L.N. Reshetova, I.A. Presniakov, E.V. Dikarev, M. Baitinger, F. Haarmann, W. Schnelle, M. Baenitz, Y. Grin, A.V. Shevelkov, Solid State Sci. 7 (2005) 957–968.
[45] M. Christensen, B.B. Iversen, Chem. Mater. 19 (20) (2007) 4896–4905.
[46] S. Yamanaka, E. Enishi, H. Fukuoka, M. Yasukawa, Inorg. Chem. 39 (1) (1999) 56–58.
[47] K. Akai, T. Uemura, K. Kishimoto, T. Tanaka, H. Kurisu, S. Yamamoto, T. Koyanagi, K. Koga, H. Anno, M. Matsuura, J. Electron. Mater. 38 (7) (2009) 1412–1417.
[48] K. Suekuni, M.A. Avila, K. Umeo, H. Fukuoka, S. Yamanaka, T. Nakagawa, T. Takabatake, Phys. Rev. B 77 (23) (2008) 235119.
[49] A. Bentien, B.B. Iversen, J.D. Bryan, G.D. Stucky, A.E.C. Palmqvist, A.J. Schultz, R.W. Henning, J. Appl. Phys. 91 (9) (2002) 5694–5699.
[50] W.G. Gou, S.Y. Rodriguez, Y. Li, J.H. Ross, Phys. Rev. B 80 (14) (2009) 144108.
[51] T. Tanaka, T. Onimaru, K. Suekuni, S. Mano, H. Fukuoka, S. Yamanaka, T. Takabatake, Phys. Rev. B 81 (16) (2010) 165110.